RSC Applied Polymers

PAPER

View Article Online
View Journal | View Issue

Cite this: *RSC Appl. Polym.*, 2025, **3**, 1553

Light-induced foldable materials with 3D-gold nanorod assemblies enable large area plasmonic hot-spot generations

Munire Derebasi,[a] Gorkem Liman,[a] Kubra Ozkan Hukum,[a] Emrecan Yildiz,[a] Poyraz Ada Demirel[a,b] and Gokhan Demirel *[a]

Foldable platforms have huge potential in the field of plasmonic engineering thanks to their ability to dynamically reconfigure surface geometries, enabling precise spatial control over nanoscale electromagnetic interactions. Herein, we demonstrate the design and fabrication of light-induced foldable polystyrene (PS) platforms functionalized with plasmonic nanostructures for dynamic control of electromagnetic hot-spot generation and surface-enhanced Raman scattering (SERS) applications. The self-folding behavior of the platforms was actuated *via* infrared (IR) irradiation, with folding angles modulated by hinge geometry and exposure time. Multi-armed PS platforms were engineered to transform from 2D to 3D configurations, enabling precise spatial localization of analyte molecules through geometric reconfiguration. Plasmonic hot-spot generations were investigated by decorating the platform surfaces with colloidal gold nanoparticles (AuNPs), nanourchins (AuNOs), and nanorods (AuNRs), as well as through the integration of 3D-oriented AuNR assemblies fabricated *via* the oblique angle deposition method. SERS measurements using methylene blue (MB) demonstrated substantial signal enhancements upon folding, with 3D-AuNR assemblies yielding superior performance due to their anisotropic and ordered architecture. A proof-of-concept application of pesticide detection from a tomato surface validated the integrated platform's capabilities for remote actuation, target collection, and ultrasensitive detection. This work highlights the potential of programmable polymeric actuators as scalable, untethered sensing devices for real-world analytical applications.

Received 23rd July 2025,
Accepted 10th September 2025

DOI: 10.1039/d5lp00229j

rsc.li/rscapplpolym

Introduction

Foldable materials have emerged as a versatile and powerful platform for realizing mechanically reconfigurable systems in diverse fields, ranging from soft robotics[1–5] and biomedical devices[6–10] to deployable electronics[11–13] and plasmonics.[14–16] These systems leverage external stimuli, such as thermal,[17,18] electrical,[19,20] optical,[21,22] or magnetic fields,[23,24] to induce controlled out-of-plane deformations, enabling the transformation of two-dimensional (2D) structures into three-dimensional (3D) architectures. Among various foldable materials, polystyrene (PS) offers significant advantages due to its low-cost processability, programmable actuation behavior, and compatibility with scalable fabrication methods. Considering these advantages, controlled folding of the pre-strained PS sheets with colored hinges using a light source has been previously reported in the literature.[25–28] As these materials absorb light, the temperature of the colored areas increases due to the heat generated by the light, and folding occurs when the polymer reaches the glass transition temperature of ~102 °C.

The integration of foldable materials with plasmonic nanostructures presents a promising route toward dynamic plasmonic hot-spot engineering, which plays a key role in the fields of surface-enhanced Raman spectroscopy (SERS) and other plasmonic sensing techniques.[29,30] By bringing plasmonic nanomaterials into close proximity during folding, such hybrid systems can create and modulate hot-spots on demand, allowing real-time tuning of electromagnetic field intensities and sensing capabilities. Recent advances have demonstrated proof-of-concept strategies in combining flexible substrates with plasmonic elements, but challenges remain in achieving precise spatial control, scalable fabrication, and multifunctional actuation. Considering the great potential and advantages of foldable materials, we recently demonstrated that the folding of a pre-strained polystyrene (PS) sheet decorated with plasmonic spherical gold nanoparticles (AuNPs) enables hot-

[a]*Bio-inspired Materials Research Laboratory (BIMREL), Department of Chemistry, Gazi University, 06500 Ankara, Turkey. E-mail: nanobiotechnology@gmail.com*
[b]*Nesibe Aydın High School, 06800 Ankara, Turkey*

spot formations by controlling the temperature distribution on the material.[31] The fabricated platforms were able to demonstrate a Raman signal enhancement due to the folding of their arms. However, this work raises an important question about how nanoparticle shapes and orientations on the surfaces affect the hot-spot formations to enhance the Raman signal intensities.

In this study, we advance the concept further by exploring how the morphology of colloidal gold nanostructures, such as nanourchins and nanorods, affects hot-spot generation efficiency. More importantly, we integrate an oblique angle deposition (OAD) technique to fabricate 3D-oriented Au nanorod assemblies directly onto foldable platforms, demonstrating a novel strategy for constructing anisotropic and spatially ordered plasmonic structures and hot-spot engineering that cannot be achieved through conventional methods. Through detailed SERS analyses using methylene blue (MB) as a probe molecule, we demonstrate significant signal amplification driven by folding-induced large-area hot-spot formation. Additionally, we demonstrate a proof-of-concept investigation of untethered analyte collection and detection from a fruit surface using magnetically guided, thermally foldable platforms. Overall, our work establishes a scalable and multifunctional approach for hot-spot engineering using mechanically reconfigurable materials. This strategy holds promise for developing next-generation plasmonic systems with dynamic sensing, adaptive optics, and on-demand molecular detection capabilities.

Results and discussion

To investigate the light-induced folding behavior of PS sheets, we fabricated samples with a central black hinge of variable width through a commercially available laser printer and subjected them to infrared (IR) irradiation using a 250 W IR lamp (Fig. 1A). The folding behavior was observed and quantified over time using both optical and infrared (IR) thermal

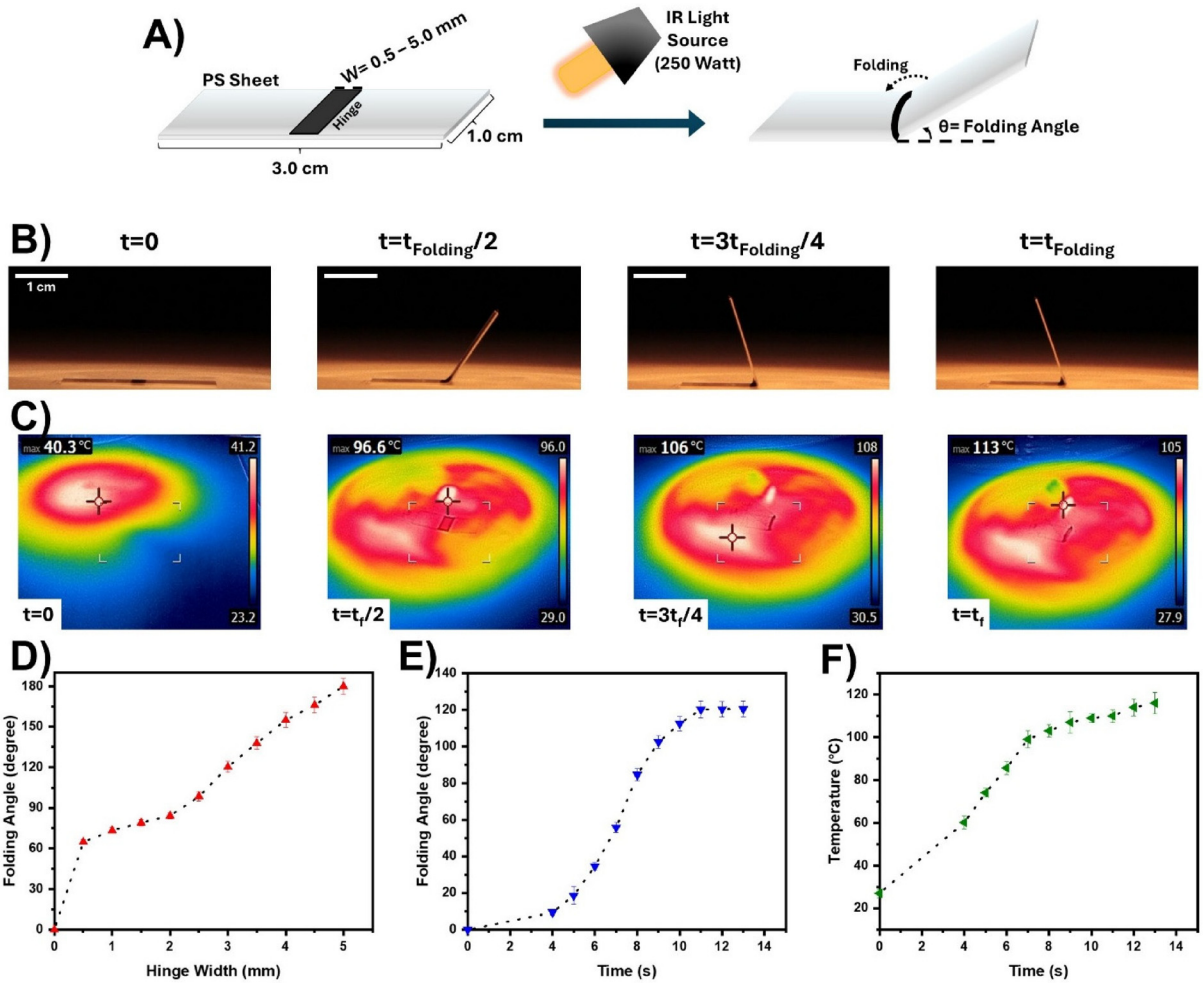

Fig. 1 Schematic illustration of the fabrication and folding process of a PS platform (A). Optical (B) and thermal camera (C) images of a 2D PS platform with a black colored hinge (3.0 mm width) under IR light illumination (250 W). Folding angles of 2D PS platforms as a function of hinge width (D). Folding angles of 2D PS platforms with a 3.0 mm hinge width as a function of time (E), and temperature changes on a PS platform under IR light illumination as a function of time (F).

imaging. Upon exposure to IR light, the PS sheet underwent progressive folding at the location of the black hinge due to localized heating (Video S1). Optical side-view images captured at four representative time points for platforms with 3 mm hinge width (Fig. 1B) show that the initially flat sheet (t = 0) began to bend upward at the hinge. The folding angle increased with time, reaching a folding angle of ~120°, which is desired for further plasmonic applications. Thermal imaging of the folding process in Fig. 1B (Fig. 1C) confirmed a localized increase in temperature at the hinge region. The hinge temperature rose rapidly from ~40.3 °C to 113 °C at t = t_f, while the surrounding areas remained comparatively cooler. It should be noted that the maximum temperature of ~113 °C was localized only in the black ink-coated hinge regions, where folding is intended to occur. In the rest of the platform, the temperature remained significantly lower, typically in the 40–80 °C range. Quantitative analysis of the thermal images revealed a strong correlation between temperature increase and the extent of folding. As shown in Fig. 1F, the hinge temperature increased rapidly within the first 10 seconds of IR exposure, plateauing at ~113 °C around 12–13 seconds. This temperature profile mirrored the temporal evolution of the folding angle (Fig. 1E), which exhibited a sigmoidal increase over time. Initially, folding was negligible, followed by a sharp increase between 4 and 10 seconds, and finally a plateau as the folding angle approached a maximum of ~120°. To determine the influence of hinge geometry on folding behavior, we systematically varied the hinge width from 0.5 mm to 5.0 mm. As shown in Fig. 1D, the final folding angle increased monotonically with hinge width. Narrow hinges (≤1 mm) resulted in minor deformation (~20°–40°), while wider hinges (≥4 mm) enabled nearly complete folding, reaching angles approaching 180°. This suggests that, as expected, wider hinges absorb more IR energy, leading to greater localized heating and more pronounced folding.[27,31] These findings collectively demonstrate that both hinge width and thermal exposure time critically govern the folding behavior of PS sheets. The combination of optical and thermal analysis confirms that IR-induced softening and shrinkage at the hinge drive the self-folding process. Considering these results, PS platforms with 3.0 mm hinge width were chosen for plasmonic engineering studies.

To enable precise spatial control over plasmonic hot-spot formation, we developed a series of multi-armed polymeric platforms capable of self-folding into three-dimensional (3D) geometries upon IR light activation. The platform designs included two-, three-, and four-armed configurations, each engineered to fold symmetrically toward a central apex, thereby reducing the inter-arm spacing. This proximity is critical for the enhancement of localized electromagnetic fields through plasmonic coupling, which is highly sensitive to nanoscale distances between metallic or functional surfaces.[32,33] The platforms were fabricated from PS sheets patterned with black ink at specific hinge regions. This colored zone on PS absorbs much more and faster IR radiation than the uncolored area, resulting in softening and shrinking the polymer locally, driving out-of-plane folding along the predefined hinge lines. This approach leverages the folding mechanism demonstrated in our previous characterization (see Fig. 1) to construct complex geometries through simple 2D-to-3D transformations. Fig. 2A shows optical images capturing the folding dynamics for each platform *versus* time. It should be noted that the hinge width was kept constant at 3 mm for each platform. Initially, all designs were flat, with arms extending radially from a central junction. Upon IR irradiation, progressive folding was observed, beginning at ~20 seconds and continuing until complete folding occurred between 41 and 49 seconds, depending on the number of arms. The two-armed structure exhibited a relatively fast folding process, completing its transformation within ~41 seconds (Video S2). The three-armed and four-armed platforms followed a similar trend, reaching their final folded geometries within ~43 and ~49 seconds, respectively (Videos S3 and S4). Each platform achieved a pyramid-like shape, with the arms lifting upward and converging near the center. This behavior demonstrates successful actuation and the robustness of the hinge design across multiple configurations. To evaluate the quality of the final folded structures, Fig. 2B shows scanning electron microscopy (SEM) images of the resulting 3D geometries. In each case, the arms are seen to be well-aligned and uniformly folded along the designed hinge lines, forming sharp creases and narrow gaps at the junction points. For the two-armed platform, the two faces form a "tent-like" structure with a small, well-defined apex. The three- and four-armed platforms form more complex pyramidal shapes, with all arms neatly folded inward and meeting at a central point. The SEM images confirm the structural integrity and symmetry of the folding process, which are crucial for ensuring consistent plasmonic interactions. Thermal behavior during folding was monitored using a real-time infrared (IR) camera, as shown in Fig. 2C. For the two-armed platform, thermal images reveal a consistent and localized increase in temperature at the black-inked hinge regions. The initial temperature (~33 °C at t = 0) increases rapidly, reaching ~87 °C by 41 seconds, in agreement with the optical folding timeline. The highest temperature zones (indicated in red) coincide with the inked hinge regions, confirming that heat is effectively confined to the intended actuation sites. This controlled thermal profile is essential for inducing predictable folding without unwanted deformation in adjacent regions. The nearly symmetrical thermal distribution across both arms also reflects uniform energy absorption, which is necessary for synchronized folding and stable final geometry. Together, these results validate the design and performance of thermally foldable multi-armed polymeric platforms for hot-spot manipulation. The demonstrated ability to achieve tight, symmetric folding with fine spatial control over arm positioning highlights the promise of this strategy for plasmonic applications. In particular, the tunability of arm number, folding angle, and hinge geometry opens avenues for the fabrication of reconfigurable optical systems, sensors, and nanoscale energy concentrators that rely on dynamic control of inter-surface distances.

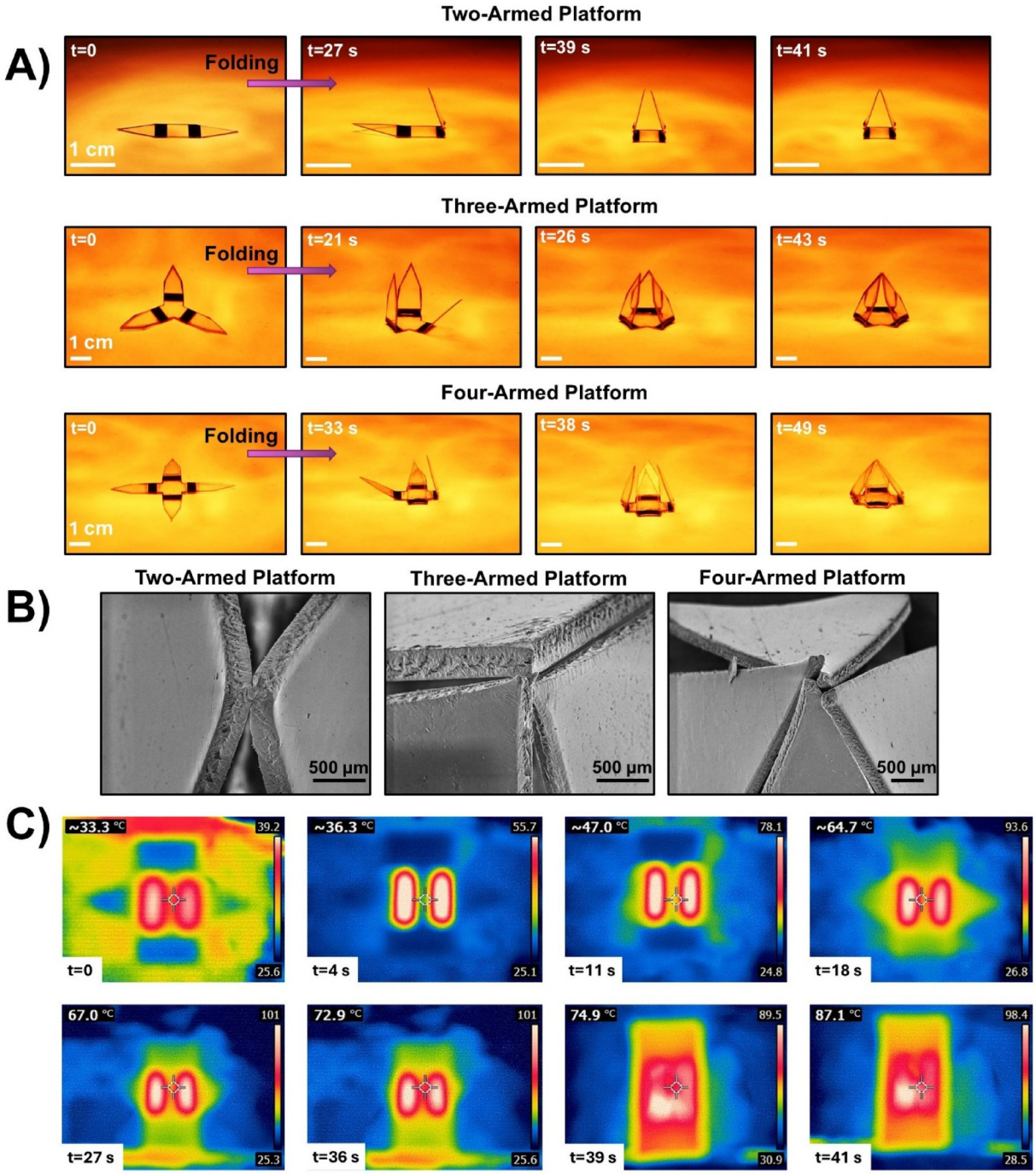

Fig. 2 Snapshot images of the 2-, 3-, and 4-armed PS platforms folding under IR light illumination (250 W) (A). SEM images of the folded 2-, 3-, and 4-armed PS platforms (B). Thermal camera images of the folding process of a 2-armed PS platform with time (C).

To functionalize the foldable PS platforms for plasmonic hot-spot applications, three types of colloidal gold nanostructures (*i.e.*, spherical gold nanoparticles (AuNPs), gold nanourchins (AuNOs), and gold nanorods (AuNRs)) were synthesized and characterized. These nanostructures were selected due to their tunable localized surface plasmon resonance (LSPR) properties and their capacity to enhance electromagnetic fields when positioned in close proximity. The TEM images revealed that the spherical AuNPs displayed uniform morphology with average diameters of ~15–20 nm, consistent with colloidal synthesis (Fig. 3A-i). The AuNOs show branched architectures with multiple sharp edges, typical of high-index facets and favorable for hot-spot generation due to their tip-enhanced field localization (Fig. 3A-ii). In contrast, the AuNRs exhibited an elongated shape with well-defined aspect ratios (length ≈ 70–120 nm, width ≈ 25–40 nm), resulting in aniso-

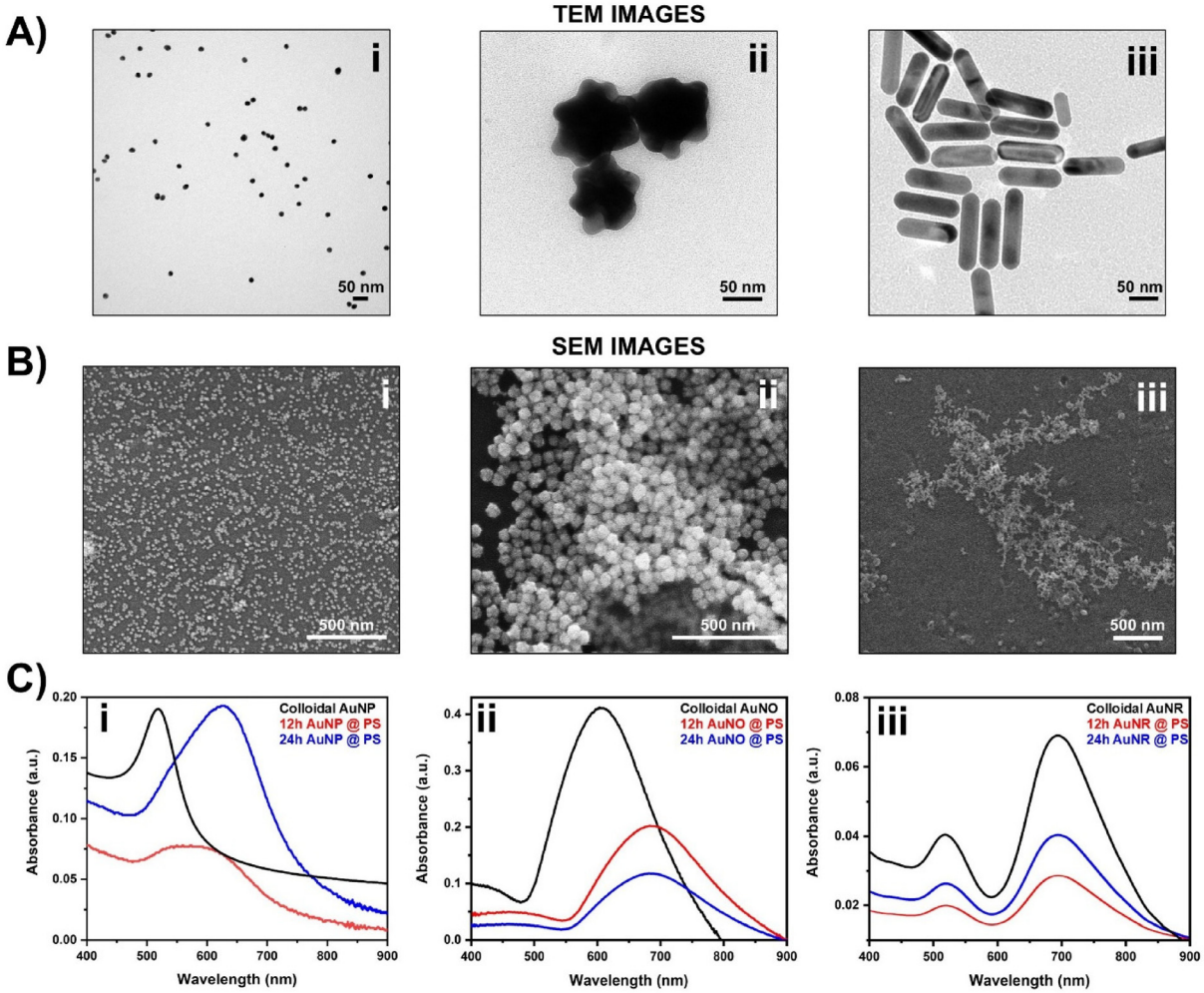

Fig. 3 TEM images of synthesized colloidal AuNPs (i), AuNOs (ii), and AuNRs (iii) (A). SEM images of the AuNP- (i), AuNO- (ii), and AuNR- (iii) decorated PS platforms for 24 h retention time periods (B). UV-vis spectra of AuNP- (i), AuNO- (ii), and AuNR- (iii) decorated PS platforms with different retention time periods (C).

tropic optical behavior (Fig. 3A-iii). Synthesized plasmonic nanoparticles were then decorated on the arms of the PS platforms before light illumination. In light of our results, 2-armed PS platforms were chosen for plasmonic engineering studies due to their producible folding behavior and easy fabrication. To adhere synthesized colloidal Au nanostructures, the 2-armed PS platforms were first functionalized with a PDOP layer with a ~10 nm thickness through the oxidation of dopamine molecules under an alkaline medium.[31] After the PDOP film functionalization of the platforms, the gold nanostructures with varying shapes were immobilized on the arms with different particle densities by controlling the retention time (12 h–24 h). SEM images of the fabricated films for a 24 h retention time are given in Fig. 3B. For a 12 h retention time, neither AuNPs nor other gold structures form a homogeneous surface coating on the PS. Therefore, we have chosen a 24 h retention time for nanoparticle functionalization of the platforms. Even at 24 h, although the AuNPs formed a homogeneous coating on the surfaces with a density of 4.2×10^9 nanoparticles per cm^2 (Fig. 3B-i), both AuNOs and AuNRs only formed aggregation-like structures (Fig. 2B-ii and iii). The modified PS platforms were also characterized by UV-vis. For AuNPs and AuNOs functionalized platforms, the LSPR absorption maximums for the platform were significantly red-shifted with respect to that of as-synthesized AuNPs and AuNOs in solution (Fig. 3C-i and ii), most likely a result of dense film formation on the platforms.[34] However, platforms functionalized with AuNRs show no LSPR shifting; only their adsorption intensities increase depending on the retention time, possibly due to the inhomogeneous film formation (Fig. 3C-iii).

Next, we evaluated the hot-spot formation ability upon folding for the fabricated platforms in detail using surface-enhanced Raman scattering (SERS) analysis. In the investigations, methylene blue (MB, 1×10^{-3} M) was used as the Raman reporter molecule. To eliminate concentration-related variations arising from platform folding, the aqueous solution of MB was drop-cast onto one side of the polystyrene (PS) platforms with functionalized gold nanostructures. All Raman

measurements were carried out under a wavelength of 785 nm (1.58 eV), at which neither the MB molecule nor the PS platform demonstrates electronic transitions.[31,35,36] First, the Raman spectrum was obtained from the AuNP-functionalized PS platform before folding (black spectrum in Fig. 4A-i). Characteristic Raman peaks for MB were obtained at 447, 1174, 1391, and 1617 cm^{-1}. After infrared (IR) illumination, the platform arms underwent folding, leading to physical contact and the formation of plasmonic hot-spots in a large area. This structural rearrangement resulted in a substantial enhancement of the Raman signal across all characteristic MB peaks. Specifically, for the platform functionalized with AuNPs, the intensities of the peaks at 447 and 1617 cm^{-1} increased by factors of 15 and 26, respectively, compared to the unfolded configuration (Fig. 4A-i). For platforms incorporating AuNOs and AuNRs, the enhancements were even more pronounced, reaching 8.5-fold (447 cm^{-1}) and 28.2-fold (1617 cm^{-1}) for AuNOs, and 29.7-fold (447 cm^{-1}) and 28.3-fold (1617 cm^{-1}) for AuNRs (Fig. 4A-ii and iii). These enhancements are attributed to the increased physical contact between the folded arms, which facilitates a greater density of probe molecule adsorption and more efficient electromagnetic field localization in the hot-spot region.[30] The intensified light–matter interactions at these junctions generate strong local electromagnetic fields accessible to nearby analyte molecules, thereby significantly boosting the Raman signal.[37] Notably, while hot-spots in the absence of external stimuli are confined to the nanoscale gaps between plasmonic nanoparticles, folding-induced contact under light illumination produces hot-spots over broader interfacial regions. It should be noted that all Raman measurements were conducted under identical experimental conditions, including laser illumination area and optical configurations, for both folded and unfolded states to ensure comparability. To further elucidate hot-spot distribution, Confocal Raman microscopy equipped with mapping software (785 nm laser, 10× objective) was employed to analyze the platforms in the folded state (Fig. 4B). Over 1000 Raman spectra were collected in a radial pattern from the outer edge toward the center of the folding junction. Two-dimensional Raman mapping revealed a progressive increase in the intensity of the MB peaks at 447 and 1617 cm^{-1} toward the central joint, confirming localized hot-spot formation at the points of physical contact.

To overcome the limitations associated with randomly distributed colloidal gold nanostructures, we fabricated 3D-oriented gold nanorod (AuNR) assemblies on the PS substrates *via* oblique angle physical vapor deposition (OAD) technique.[38–41] As schematically illustrated in Fig. 5A, gold was thermally evaporated onto the PS platform positioned at a 10° deposition angle relative to the vapor flux, enabling the aniso-

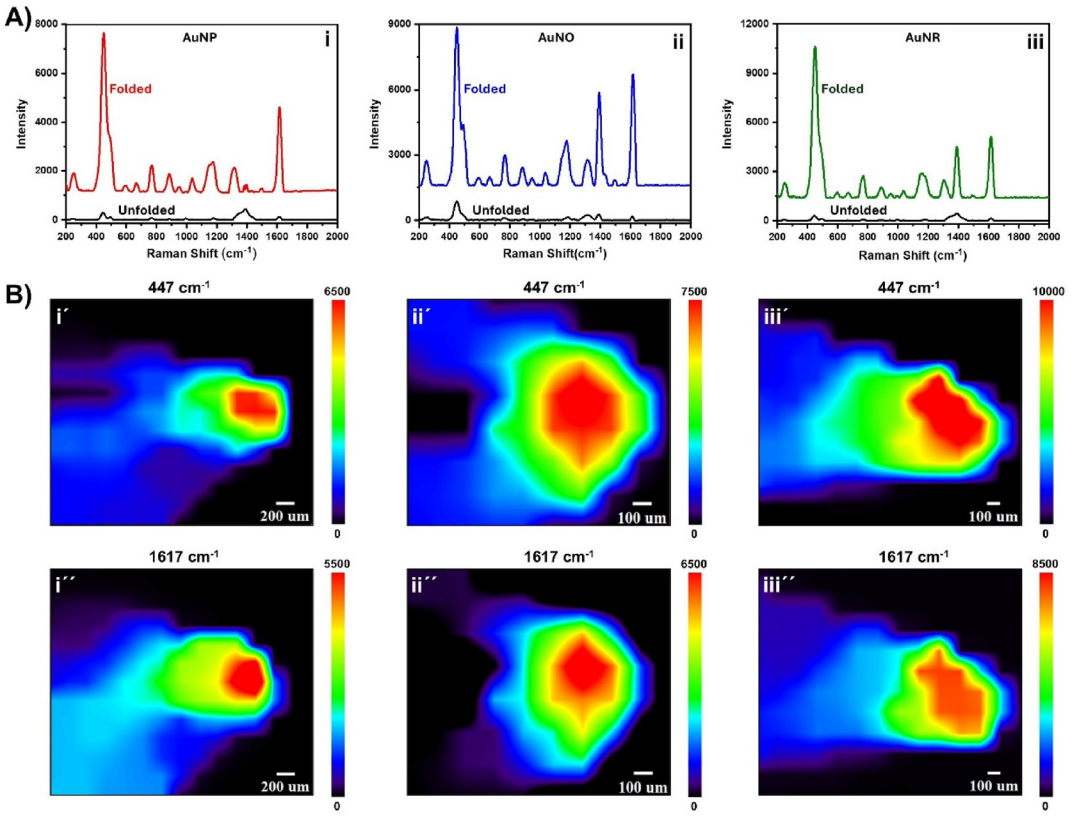

Fig. 4 SERS spectra of MB collected from AuNP- (i), AuNO-, and AuNR-(iii) decorated 2-armed PS platforms before and after folding (A). 2D SERS Raman mapping of the folded AuNP- (i′ and i″), AuNO- (ii′ and ii″), and AuNR-(iii′ and iii″) decorated 2-armed PS platforms for the 447 and 1617 cm^{-1} peaks of MB (B).

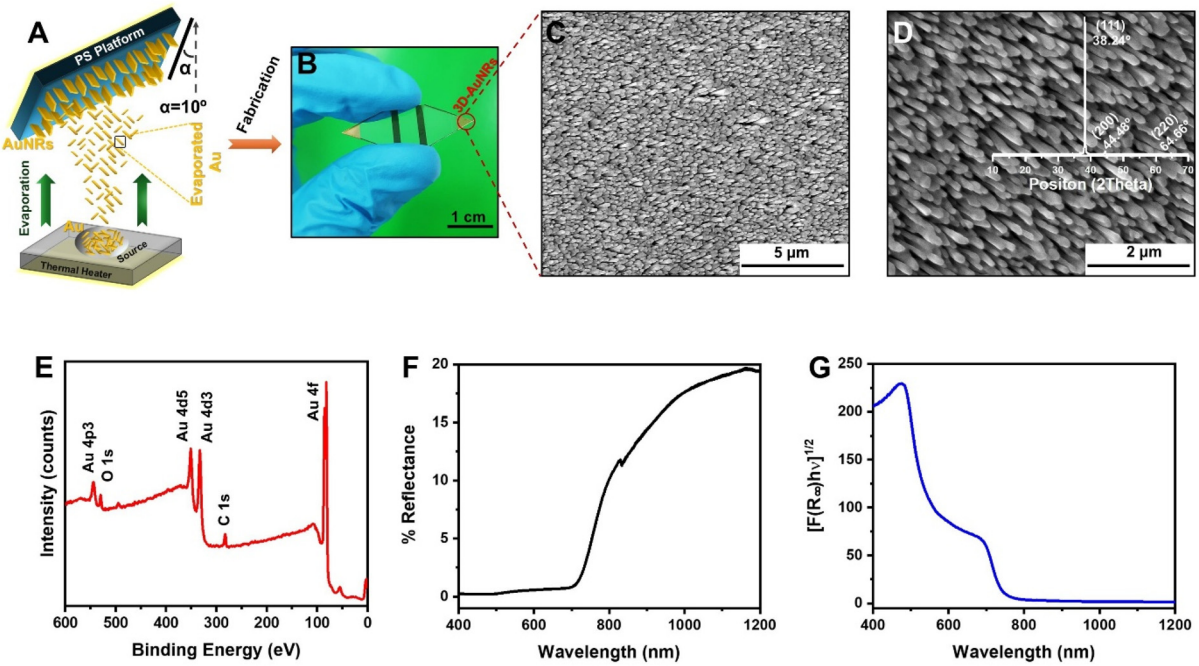

Fig. 5 Schematic illustration of the fabrication process of 3D-AuNR assemblies on a PS platform (A). Optical image of a fabricated PS platform with 3D-AuNR assemblies (B). SEM images of 3D-AuNR assemblies on a PS platform (C and D) (inset shows the XRD pattern of AuNR assemblies deposited on the PS platform). XPS spectrum of 3D-AuNR assemblies deposited PS platform (E). UV-Vis reflectance spectrum (F) and Kubelka–Munk function (G) of 3D-AuNR assemblies deposited PS platform.

tropic growth of vertically oriented nanorods due to shadowing effects intrinsic to the OAD method. An optical image of the fabricated platform is shown in Fig. 5B, demonstrating uniform deposition over a centimeter-scale area, which is critical for scalable and reproducible plasmonic device integration. Surface morphology of the deposited 3D-AuNR assemblies was assessed using SEM. At lower magnification (Fig. 5C), the AuNRs appear densely packed and vertically oriented across the PS platform surface. Higher magnification imaging (Fig. 5D) confirms the formation of tilted nanorod assemblies with consistent orientation and spacing, exhibiting widths in the range of 100–160 nm and lengths of 800–1100 nm. Note that the deposited AuNR packing is heterogeneous with no discernible long-range order in SEM. The X-ray diffraction (XRD) pattern (inset of Fig. 5D) reveals distinct diffraction peaks corresponding to the (111), (200), and (220) planes of crystalline gold, indicating high crystallinity and preferential orientation along the (111) facet. X-ray photoelectron spectroscopy (XPS) analysis (Fig. 5E) further verifies the elemental composition of the deposited nanostructures. Distinct peaks corresponding to Au 4f, Au 4d, and Au 4p states confirm the presence of metallic gold, while minor signals from C 1s and O 1s are attributed to the underlying PS substrate and surface adsorbates. Optical characterization was performed using UV-Vis reflectance spectroscopy (Fig. 5F), revealing a broad plasmonic response extending from the visible to the near-infrared region, a signature of longitudinal plasmon modes supported by anisotropic AuNRs. The corresponding Kubelka–Munk function plot derived from the reflectance data (Fig. 5G) indicates strong light absorption and enhanced electromagnetic activity within the visible spectrum, which is essential for plasmonic field enhancement applications.

To evaluate the hot-spot formation capabilities of the fabricated PS platforms with 3D-AuNR assembly, SERS measurements were performed using methylene blue (MB), similar to other platforms with colloidal Au nanostructures. As shown in Fig. 6A, the Raman spectra acquired from the folded substrate with 3D-Au nanorod (AuNR) assemblies exhibit significantly amplified signal intensity compared to the unfolded state across the entire spectral window (200–2000 cm^{-1}). Notably, the peaks at 447 cm^{-1} and 1617 cm^{-1}, corresponding to the C–N–C skeletal stretching and aromatic C–C stretching modes of MB, respectively, are strongly enhanced in the folded configuration as expected. The Raman signal enhancement indicates effective electromagnetic field confinement at the nanorod interfaces, facilitated by the mechanical deformation of the flexible substrate. To evaluate the SERS performance of the 3D-AuNR assemblies against colloidal Au nanostructures, we systematically compared the SERS signal intensities across different nanostructure types: AuNPs, AuNOs, AuNRs, and 3D-AuNR assemblies. Fig. 6B and C present the quantified SERS intensities at 447 cm^{-1} and 1617 cm^{-1}, respectively, for each platform in both unfolded and folded states. While all platforms exhibit some Raman signal enhancement upon folding, the 3D-AuNR assemblies outperform the colloidal counterparts by a considerable margin. This enhancement is

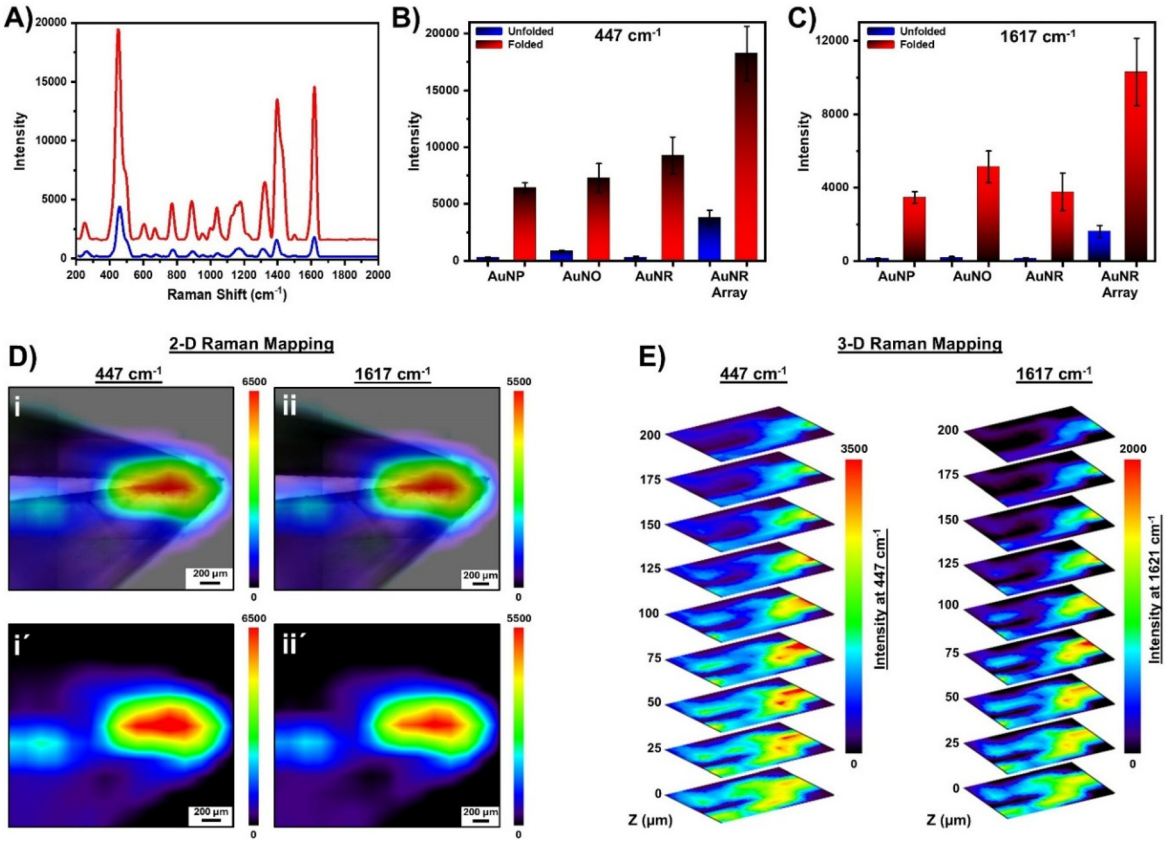

Fig. 6 (A) SERS spectra of MB on 3D-AuNR assemblies deposited PS platform before and after folding. Raman intensity histograms of 447 cm^{-1} (B) and 1617 cm^{-1} (C) peaks derived from SERS spectra in (Fig. 4A) and (Fig. 6A). (For all experiments, the concentration of MB was 10^{-3} M.) (D) 2D SERS Raman mapping of the folded 3D-AuNR assemblies deposited PS platforms for the 447 cm^{-1} (i and i′) and 1617 cm^{-1} peaks (ii and ii′) of MB (the first figures (i and ii) are the overlaying figures that were produced using real platform pictures obtaining from Raman microscope and 2D SERS Raman mappings of the collected analyte molecules on the platforms for the 447 and 1617 cm^{-1}). (E) 3D Raman spatial mapping of the folded 3D-AuNR assemblies deposited on the PS platform, showing different focal planes along the *z*-axis for 447 and 1617 cm^{-1} peaks of MB.

attributed to the anisotropic geometry, and dense spatial arrangement of the AuNRs grown *via* oblique angle deposition, which together promote the generation of densely packed "hot-spots" upon platform folding. Specifically, the folded 3D-AuNR assemblies yields up to a 5-fold increase in SERS intensity compared to folded colloidal AuNRs and over 10-fold enhancement relative to unfolded colloidal structures. These findings demonstrate the critical role of nanoscale ordering and orientation in modulating hot-spot formation. Additionally, to spatially visualize the hot-spot formations across the platforms, the 2D Raman mapping was carried out from outside the joint point of the PS platforms to the center of the joint by collecting more than 1000 Raman spectra. As expected, MB Raman signals (447 and 1617 cm^{-1}) gradually increased from outside of the joint point to the center of the joint point, indicating obvious hot-spot engineering (Fig. 6D). To further elucidate the depth profile of SERS activity, 3D Raman mapping was performed (Fig. 6E) by stacking Raman slices along the *Z*-axis. The data reveal a layered architecture of signal distribution within the folded substrate, extending up to 200 µm in depth. The resultant spatial map indicates that hot-spot formations are denser towards the center of the joint as compared to the other areas. This hot-spot formation is likely a result of interpenetrating nanorod domains formed during folding, which create multiple vertical hot-spot formations, thereby expanding the active sensing volume. Overall, these results validate that the OAD-fabricated, foldable 3D-AuNR assemblies not only overcome the intrinsic limitations of randomly distributed colloidal systems but also enable the mechanical tuning of SERS performance through controlled deformation.

To demonstrate the practical applicability and sensing capability of the fabricated platforms, a proof-of-concept experiment was conducted, targeting the collection and detection of analyte molecules from a real-world surface. Our objective was to validate the integration of actuation, transport, and sensing within a single, untethered system. To enable remote actuation and directional control, the two-armed PS platforms were functionalized post-fabrication with small magnetic films (2 mm in diameter and 0.4 mm in thickness). These films allowed precise manipulation of the platforms under an external magnetic field (~150 mT) without direct contact, facilitat-

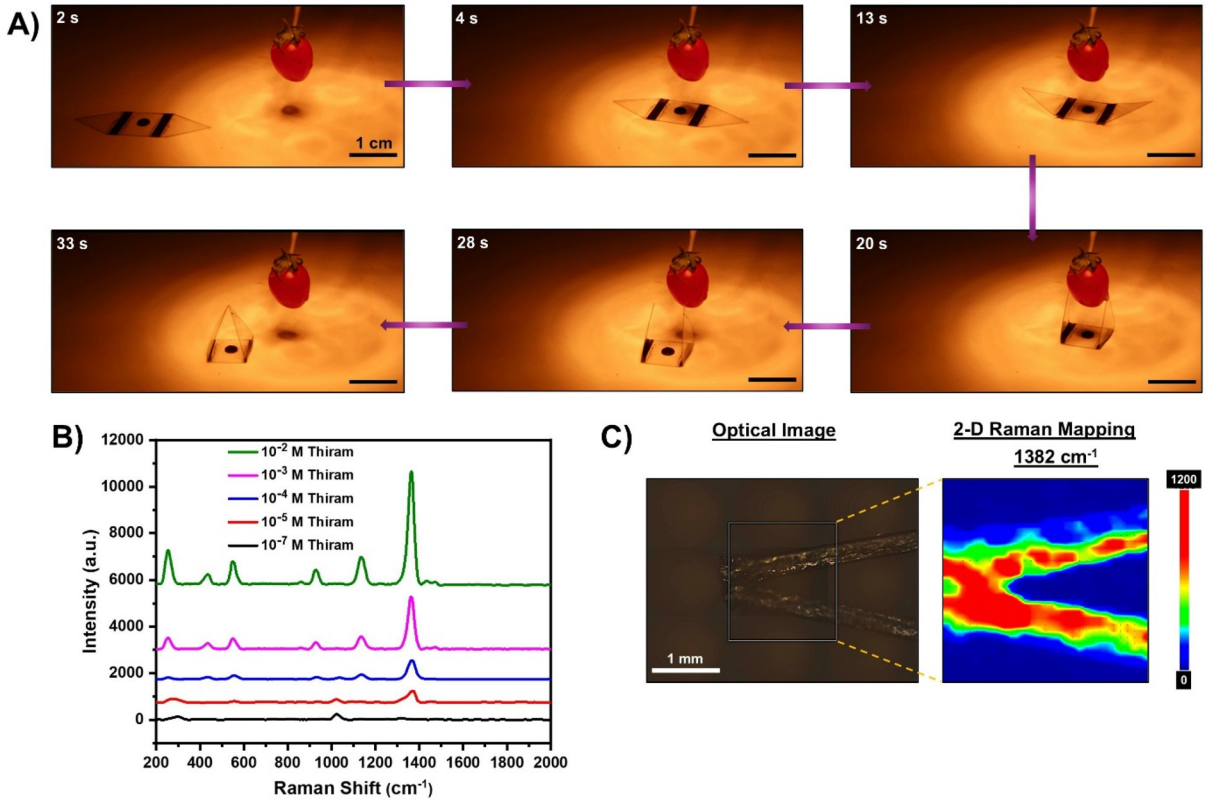

Fig. 7 (A) Snapshot images of sample collection from Thiram-impregnated cherry tomato using two-armed polymeric platforms. (B) SERS spectra of Thiram with different concentrations collected from a target using two-armed PS platforms. (C) 2D SERS Raman mappings of the collected Thiram molecules on the platforms for the 1382 cm^{-1}.

ing their deployment in sensitive or hard-to-reach environments. Thiram, a commonly used pesticide and Raman-active molecule, was chosen as the target analyte to evaluate the system's sensitivity and environmental relevance.[42,43] A cherry tomato surface was employed as a model fruit substrate, onto which known concentrations of Thiram were applied. As depicted in Fig. 7A, the actuator platform was initially magnetically guided toward the tomato (2–13 seconds). Upon reaching the target, IR illumination was used to induce the controlled folding of PS platforms (20–33 seconds) (Video S5). This motion not only enabled the wrapping of the target surface but also enhanced surface contact and local pressure, facilitating efficient uptake of analyte molecules onto the SERS-active regions. Following analyte collection, the platform was transported back to the sensing region under magnetic guidance. The folding of the platform promotes the formation of hot-spots by bringing plasmonic nanostructures into close proximity. SERS measurements were then performed, as shown in Fig. 7B, and revealed clear, concentration-dependent spectral signatures of Thiram (10^{-2} to 10^{-7} M), demonstrating the high sensitivity and dynamic range of the system. Notably, the intensity of the characteristic Thiram peak at 1382 cm^{-1} (C–S–S stretching) served as a reliable marker for quantification. To spatially validate analyte distribution and hot-spot formation, 2D Raman mapping at 1382 cm^{-1} was conducted and is shown in Fig. 7C. The mapping results confirmed strong Raman signal localization along the folding axis of the actuator arms.

Conclusions

In this work, we have demonstrated the fabrication and functionalization of polystyrene (PS) platforms capable of undergoing self-folding transformations upon infrared (IR) irradiation. These polymeric actuators exploit localized heating at ink-printed hinge sites to achieve controlled 2D-to-3D transitions, enabling precise spatial modulation of surface geometry. The folding behavior was systematically characterized as a function of hinge width and exposure time, with optimal folding angles achieved at 3 mm hinge widths. This tunability allowed the construction of multi-armed architectures with reproducible folding dynamics and structural symmetry. By integrating colloidal AuNPs, AuNOs, and AuNRs as well as obliquely deposited 3D-AuNR assemblies, we endowed the foldable platforms with tailored plasmonic properties. These functionalized systems demonstrated significant Raman signal enhancement upon folding, driven by the formation of plasmonic hot-spots at inter-arm joint points. Notably, platforms featuring 3D-AuNR assemblies exhibited superior perform-

ance, owing to their anisotropic geometry, dense, and 3D-oriented arrangement, which amplified local field confinement. Raman mapping further validated the large-area hotspot generations within the folded geometries. The versatility and practicality of the system were highlighted through a proof-of-concept demonstration, wherein magnetically controllable, foldable platforms were used for the remote sample collection and detection of thiram pesticide residues from the surface of a cherry tomato. This fully untethered process from actuation and sampling to sensing underscores the potential of these devices for real-world applications. Looking ahead, the demonstrated approach opens several exciting avenues for future research and technological development. First, the modularity of the design enables the integration of additional functionalities such as chemical specificity through selective receptors, or wireless triggering mechanisms using photothermal or RF sources. Second, the concept could be extended to other flexible substrates and nanoparticle types to further tailor optical responses, mechanical behavior, and chemical compatibility. Third, miniaturization of the platforms and optimization of folding kinetics could facilitate their deployment in microfluidic or biomedical environments, such as implantable diagnostics or responsive drug delivery systems. Additionally, with further engineering, these foldable plasmonic systems could serve as building blocks for dynamic optical metamaterials, tunable photonic devices, or smart environmental sensors. The ability to control plasmonic interactions *via* mechanical deformation introduces a new paradigm in the design of reconfigurable nanophotonic systems. Overall, this work lays the foundation for next-generation, shape-morphing analytical platforms that combine structural programmability, plasmonic functionality, and autonomous operation.

Experimental

Fabrication of platforms

Pre-strained polystyrene (PS) sheets (Grafix; thickness: 0.27 mm) were used as the starting material for platform fabrication. Platform and hinge geometries were designed using AutoCAD software and transferred onto the PS sheets using an HP Color LaserJet M553 printer. The patterns were then manually cut using a no. 11 scalpel blade. Thermal actuation of the polymeric platforms was achieved using a 250 W infrared (IR) lamp positioned approximately 8 cm above the sample surface. This configuration ensured sufficient energy delivery for shape transformation while preserving structural integrity. The folding process was recorded using a Canon EOS 650D digital camera, and the resulting folding angles were analyzed with ImageJ software. Thermal profiles during actuation were acquired using a FLIR E6 thermal imaging camera.

Surface functionalization of PS platforms with gold nanostructures

To decorate the arms of PS platforms with colloidal Au nanostructures, samples were immersed in a dopamine hydrochloride solution (2.0 mg mL^{-1} in 10 mM Tris buffer, pH 8.5) for 3 h at room temperature.[31,44] Following thorough rinsing with deionized water and nitrogen drying, the PDOP-coated platforms were incubated in aqueous colloidal solutions of gold nanostructures for durations ranging from 12 to 24 h. The synthesis of AuNPs,[45] AuNOs,[46] and AuNRs[40] followed established protocols as described in previous literature.

For the fabrication of 3D-oriented AuNR assemblies, PS platform arms were first cleaned with ethanol and deionized water. A custom oblique angle deposition (OAD) setup integrated with a physical vapor deposition (PVD) system (NANOVAK HV, Ankara, Turkey) was employed.[38,40] Gold was evaporated at a rate of 0.1 Å s^{-1} under a deposition angle of 10°, with film thickness monitored in real time using an Inficon XTM/2 deposition controller (sensitivity: 0.5%).

SERS investigations

Surface-enhanced Raman scattering (SERS) measurements were performed using a high-resolution confocal Raman microscope (Jasco NRS-4500, Japan) with a 785 nm excitation laser and a spectral acquisition range of 200–2000 cm^{-1}. Unless otherwise stated, Raman spectra were collected using a 20× microscope objective (laser spot size: ~3 μm), laser power of 75 mW, and an exposure time of 30 s. Methylene blue (MB) was used as a Raman reporter molecule. A 5.0 μL aliquot of aqueous MB solution (1×10^{-3} M) was drop-cast onto the sample surface and allowed to dry under ambient conditions. Raman spectra were collected from a minimum of ten randomly selected positions across the dried spot to ensure reproducibility and spatial consistency.

Conflicts of interest

The authors declare no competing interests.

Data availability

The data supporting this article have been included as part of the SI. See DOI: https://doi.org/10.1039/d5lp00229j.

Acknowledgements

This work was supported by the Scientific and Technological Research Council of Turkey (TUBITAK) (grant no. 22AG056 and 221M546).

References

1 J. Liu, Y. Gao, Y.-J. Lee and S. Yang, *Trends Chem.*, 2020, **2**, 107–122.
2 E. Sachyani Keneth, A. Kamyshny, M. Totaro, L. Beccai and S. Magdassi, *Adv. Mater.*, 2021, **33**, 2003387.

3 J. C. Breger, C. Yoon, R. Xiao, H. R. Kwag, M. O. Wang, J. P. Fisher, T. D. Nguyen and D. H. Gracias, *ACS Appl. Mater. Interfaces*, 2015, **7**, 3398–3405.
4 Y. Chi, Y. Li, Y. Zhao, Y. Hong, Y. Tang and J. Yin, *Adv. Mater.*, 2022, **34**, 2110384.
5 B. Jin, H. Song, R. Jiang, J. Song, Q. Zhao and T. Xie, *Sci. Adv.*, 2018, **4**, eaao3865.
6 C. L. Randall, E. Gultepe and D. H. Gracias, *Trends Biotechnol.*, 2012, **30**, 138–146.
7 R. Fernandes and D. H. Gracias, *Adv. Drug Delivery Rev.*, 2012, **64**, 1579–1589.
8 A. Kirillova and L. Ionov, *J. Mater. Chem. B*, 2019, **7**, 1597–1624.
9 X. Li, L. Wang, Y. Li and S. Xu, *ACS Appl. Polym. Mater.*, 2023, **5**, 1585–1595.
10 A. Ingar Romero, T. Raicevic, G. Al Boustani, M. Gupta, A.-C. Heiler, L. Bichlmaier, M. Barbone, M. Becherer, D. Kiriya and S. Inoue, *ACS Appl. Mater. Interfaces*, 2025, **17**(7), 10305–10315.
11 M. J. Kim, H. S. Ryu, Y. Y. Choi, D. H. Ho, Y. Lee, A. Tripathi, J. H. Son, Y. Lee, S. Kim and M. S. Kang, *Sci. Adv.*, 2021, **7**, eabg8169.
12 W. Jo, K. Jeong, Y.-S. Park, J.-I. Lee, S. G. Im and T.-S. Kim, *Chem. Eng. J.*, 2023, **452**, 139050.
13 J. Yi, G. Zou, J. Huang, X. Ren, Q. Tian, Q. Yu, P. Wang, Y. Yuan, W. Tang and C. Wang, *Nature*, 2023, **624**, 295–302.
14 F. Diehl, S. Hageneder, S. Fossati, S. K. Auer, J. Dostalek and U. Jonas, *Chem. Soc. Rev.*, 2022, **51**, 3926–3963.
15 K. J. Si, D. Sikdar, Y. Chen, F. Eftekhari, Z. Xu, Y. Tang, W. Xiong, P. Guo, S. Zhang and Y. Lu, *ACS Nano*, 2014, **8**, 11086–11093.
16 J. Kim, J. Yeom, Y. G. Ro, G. Na, W. Jung and H. Ko, *ACS Nano*, 2024, **18**, 21364–21375.
17 W. Wei, T. Guan, C. Li, L. Shen and N. Bao, *Ind. Eng. Chem. Res.*, 2020, **59**, 2946–2952.
18 Y. Tokudome, H. Kuniwaki, K. Suzuki, D. Carboni, G. Poologasundarampillai and M. Takahashi, *Adv. Mater. Interfaces*, 2016, **3**, 1500802.
19 S. Ahmed, Z. Ounaies and E. A. F. Arrojado, *Sens. Actuators, A*, 2017, **260**, 68–80.
20 Y. Shin, M.-Y. Choi, J. Choi, J.-H. Na and S. Y. Kim, *ACS Appl. Mater. Interfaces*, 2021, **13**, 15633–15646.
21 R. Zheng, Y. Wei, Z. C. Zhang, Z. Y. Wang, L. L. Ma, Y. Wang, L. Huang and Y. Q. Lu, *Responsive Mater.*, 2023, **1**, e20230017.
22 E. Ergene, G. Liman, E. Yildiz, P. Yilgor Huri and G. Demirel, *ACS Appl. Polym. Mater.*, 2021, **3**, 3272–3277.
23 E. Ergene, G. Liman, P. Yilgor and G. Demirel, *Adv. Mater. Technol.*, 2024, **9**, 2400119.
24 K. Ozkan Hukum, G. Liman and G. Demirel, *ACS Appl. Mater. Interfaces*, 2024, **16**, 44105–44113.
25 Y. Lee, H. Lee, T. Hwang, J.-G. Lee and M. Cho, *Sci. Rep.*, 2015, **5**, 16544.
26 Y. Lee, J. Moon, J. Choi and M. Cho, *Sci. Rep.*, 2017, **7**, 1–16.
27 Y. Liu, J. K. Boyles, J. Genzer and M. D. Dickey, *Soft Matter*, 2012, **8**, 1764–1769.
28 Y. Liu, B. Shaw, M. D. Dickey and J. Genzer, *Sci. Adv.*, 2017, **3**, e1602417.
29 S. Wang, L. Arnaud, S. Essaidi, S. Blaize, S. Kostcheev, A. Bruyant, A. Hmima, Y. Hadjar, D. Macias and P.-M. Adam, *J. Opt. Soc. Am. B*, 2022, **39**, 1400–1409.
30 G. Liman, E. Ergene, E. Yildiz, K. O. Hukum, P. Yilgor Huri, A. E. Cetin, H. Usta and G. Demirel, *Adv. Intell. Syst.*, 2023, **5**, 2200420.
31 G. Liman, E. Yildiz, H. Ilhan, A. E. Cetin and G. Demirel, *Adv. Opt. Mater.*, 2021, **9**, 2100009.
32 Y. Wy, H. Jung, J. W. Hong and S. W. Han, *Acc. Chem. Res.*, 2022, **55**, 831–843.
33 X. Yang, D. Su, X. Yu, P. Zeng, H. Liang, G. Zhang, B. Song and S. Jiang, *Small*, 2023, **19**, 2205659.
34 Y. Wang, Z. Gao, Z. Han, Y. Liu, H. Yang, T. Akkin, C. J. Hogan and J. C. Bischof, *Sci. Rep.*, 2021, **11**, 898.
35 G. Demirel, R. L. Gieseking, R. Ozdemir, S. Kahmann, M. A. Loi, G. C. Schatz, A. Facchetti and H. Usta, *Nat. Commun.*, 2019, **10**, 5502.
36 I. Deneme, G. Liman, A. Can, G. Demirel and H. Usta, *Nat. Commun.*, 2021, **12**, 6119.
37 A. E. Cetin, D. Etezadi and H. Altug, *Adv. Opt. Mater.*, 2014, **2**, 866–872.
38 M. Yilmaz, H. B. Kuloglu, H. Erdogan, S. S. Cetin, M. S. Yavuz, G. O. Ince and G. Demirel, *Adv. Mater. Interfaces*, 2015, **2**, 1500226.
39 L. Kubus, H. Erdogan, E. Piskin and G. Demirel, *Soft Matter*, 2012, **8**, 11704–11707.
40 M. Yilmaz, E. Senlik, E. Biskin, M. S. Yavuz, U. Tamer and G. Demirel, *Phys. Chem. Chem. Phys.*, 2014, **16**, 5563–5570.
41 A. Uçar, E. Er and G. Demirel, *ACS Appl. Opt. Mater.*, 2024, **2**, 2551–2558.
42 M. Shafi, P. Duan, W. Liu, W. Zhang, C. Zhang, X. Hu, Z. Zha, R. Liu, C. Liu and S. Jiang, *Langmuir*, 2022, **38**, 16183–16193.
43 P. Guo, D. Sikdar, X. Huang, K. J. Si, W. Xiong, S. Gong, L. W. Yap, M. Premaratne and W. Cheng, *Nanoscale*, 2015, **7**, 2862–2868.
44 M. S. Akin, M. Yilmaz, E. Babur, B. Ozdemir, H. Erdogan, U. Tamer and G. Demirel, *J. Mater. Chem. B*, 2014, **2**, 4894–4900.
45 N. R. Jana, L. Gearheart and C. J. Murphy, *Langmuir*, 2001, **17**, 6782–6786.
46 J. Li, J. Wu, X. Zhang, Y. Liu, D. Zhou, H. Sun, H. Zhang and B. Yang, *J. Phys. Chem. C*, 2011, **115**, 3630–3637.